Advanced Functional Materials

ADVANCED FUNCTIONAL MATERIALS
www.afm-journal.de

RESEARCH ARTICLE OPEN ACCESS

Biomimetic Microfractals Based Flexible Triboelectric Nanogenerators

Amit Barua[1] | Mislav Matić[2] | Ana-Marija Pitner[1] | Rituporn Gogoi[1] | Aman Kumar[1] | Mirko Poljak[2] | Anastasia Koivikko[1] | Vipul Sharma[1]

[1]Department of Mechanical and Materials Engineering, University of Turku, Turku, Finland | [2]Computational Nanoelectronics Group, Faculty of Electrical Engineering and Computing, University of Zagreb, Zagreb, Croatia

Correspondence: Vipul Sharma (vipul.sharma@utu.fi)

Received: 10 March 2026 | **Revised:** 29 June 2026 | **Accepted:** 2 July 2026

Keywords: current density | materials science | nanogenerator | nanowire | optoelectronics | planar | power density | sheet resistance | triboelectric effect | voltage

ABSTRACT

Flexible TENGs are promising for self-powered wearables, but combining high output, mechanical compliance, and low material use remains challenging. Here, we report a biomimetic microfractal TENG (BM-TENG) inspired by leaf-skeleton vascular architectures, where the hierarchical network serves as both porous current-collector scaffold and template for triboelectric surface replication. Copper nanowires immobilized along the microfractal pathways form guided and locally bundled conductive networks, enabling a low sheet resistance of ~15 Ω sq^{-1} and >1000 fold reduction in sheet resistance compared with a planar control. Replication of the same architecture into electrospun Nylon-6 and PVDF layers creates a compliant multiscale topography that enhances charge generation. The BM-TENG delivers ~52 V open-circuit voltage, ~3.2 μA short-circuit current, and ~67.24 nC transferred charge per cycle while using 50% lower CuNW loading, compared with ~26 V, ~1.23 μA, and ~27.35 nC for the planar control. Using projected device area as the primary normalization basis, BM-TENG achieves a current density of ~3 mA m^{-2} and power density of ~136.91 mW m^{-2}, compared with ~1.13 mA m^{-2} and 135.80 mW m^{-2} for the planar control. As secondary metrics, effective-material-area normalization gives ~10 mA m^{-2} and ~456.35 mW m^{-2} for the BM-TENG. The device also maintains stable output over ~10000 cycles.

1 | Introduction

The rapid growth of flexible electronics and wearable technology has created a strong demand for lightweight, flexible, resource-efficient, and mechanically compliant energy harvesting technologies [1–7]. Among different approaches, triboelectric nanogenerators (TENGs) have emerged as a promising solution due to their ability to easily convert mechanical energy to electrical energy through contact electrification and electrostatic induction [8–18]. When two materials having different triboelectric polarities are contacted and separated with each other repeatedly, opposite charges are generated on their surface, inducing a potential difference that drives current through an external circuit. They also come with a simple structure, material versatility, and low cost. Among different categories of TENG, flexible TENGs are particularly attractive because of their capability to harvest energy from human body motion [1, 19, 20] and environmental vibrations [21], enabling power generation in everyday conditions. This is advantageous especially for the next generation of flexible and wearable devices, as flexible TENGs have the potential to serve as an independent power source for them [22–26]. The need for external batteries can be reduced or eliminated by directly integrating flexible TENGs into flexible substrates, electronic skins [27], etc. However, it is very challenging to achieve high electrical output while maintaining mechanical flexibility,

particularly in the case of prolonged contact with the human body.

Biomimetic TENGs have rapidly evolved as a key strategy for improving the performance and functionality of TENGs by drawing inspiration from natural designs and mechanisms [28]. Bioinspired surface morphologies and structural designs such as plant leaf patterns, hierarchical microstructures, and animal-inspired textures have been shown to significantly improve contact area, charge generation, and mechanical adaptability by enabling high voltage, current, and power outputs in various modes of operation [29–31]. Recent advances include leaf-templated micro-structured TENGs with robust performance and durability over many cycles, as well as bioinspired designs targeted at electronic skin and human–machine interfaces with enhanced flexibility and tactile responsiveness [32]. Among the bioinspired designs, leaf skeleton architectures can offer effective solutions due to their vascular networks composed of hierarchical and fractal structures that efficiently distribute mechanical stress and maximize surface area while minimizing material usage [33–37]. Incorporating these natural microstructures onto functional surfaces provides significant advantages over conventional planar surfaces, including enhanced electron transport pathways, improved breathability, greater flexibility, and better mechanical robustness. These hierarchical architectures can significantly enhance the output performance of TENGs by forming long-range continuous electrical pathways and high-density cross-linked networks, which are essential for efficient charge generation and transport, leading to higher current density. In addition, the fractal and porous nature of these structures promotes breathability by allowing effective air and moisture transport, which is critical for skin-attached and wearable devices. At the same time, the interconnected network helps distribute applied mechanical stress more evenly, reducing localized strain and improving mechanical durability under repeated bending and deformation.

Conductive materials are essential components in flexible TENG research for efficient charge collection and transport. 1D nanowires are particularly attractive as they are flexible and crack-resistant, making them suitable for bendable and wearable applications [38–41]. The nanowires offer high aspect ratio, large surface area, and the ability to form percolated networks [38, 42, 43]. Among metal nanowires, silver, gold, and CuNWs have been widely studied for flexible electronics [39, 40, 44]. One common challenge regarding the nanowires is agglomeration during deposition, which often leads to non-uniform coverage and degraded electrical performance. In our previous work, silver nanowires (AgNWs) were used due to their high conductivity and ease of processing [33, 35, 45], but their high cost and limited sustainability motivate the use of CuNWs as a promising alternative. More recently, nanostructured copper-based electrodes have been gaining attention as an abundant and cheaper alternative to silver. CuNWs offer electrical performance that is very close to that of silver, with only a slight difference in conductivity, but they come with significant practical advantages, like copper being vastly more abundant and available at a much lower cost than silver, making it a more economical choice for scalable electronic applications [46]. Despite offering comparable electrical conductivity at a lower cost, CuNWs are more susceptible to agglomeration and oxidation, making uniform and stable coating a key challenge for high-performance TENGs [47–49]. In this context as well, bioinspired 3D leaf-like surfaces provide an effective platform for the uniform dispersion of conductive nanomaterials [33, 35, 37]. The presence of a hierarchical vascular network enables CuNWs to be distributed evenly across the surface, forming long-range interconnected conductive pathways while suppressing agglomeration. This microfractal architecture can facilitate efficient charge transport throughout the entire device while maintaining breathability and reducing material consumption. By mimicking natural systems, the resulting conductive network also ensures stable electrical output under repeated mechanical deformation, making it highly suitable for flexible and wearable TENG applications.

In this work, we report a biomimetic microfractal triboelectric nanogenerator (BM-TENG) that integrates breathability, mechanical compliance, and enhanced electrical output through a leaf-skeleton-derived hierarchical architecture. CuNWs are employed as a lower-cost alternative to AgNWs, while the biomimetic design improves charge collection and triboelectric interaction at reduced conductive-material loading. These results demonstrate how natural microfractal architectures can guide the development of breathable and flexible triboelectric nanogenerators for next-generation self-powered systems.

We hypothesize that the leaf-skeleton microfractal architecture enhances BM-TENG performance through two complementary mechanisms: first, the hierarchical vein network acts as a current-collector scaffold that promotes guided alignment and local bundling of CuNWs, thereby reducing transport losses at low areal loading; second, replication of the same microfractal geometry into electrospun Nylon-6 and PVDF layers increases multiscale interfacial contact and charge-storage sites during triboelectric cycling. Together, these effects are expected to improve current density and power density while preserving breathability and mechanical compliance. To test this hypothesis, we benchmarked the sheet resistance of CuNWs-coated leaf skeletons against planar CuNWs coatings, used resistor-network simulations to isolate the roles of directionality and bundling, and correlated collector properties with BM-TENG electrical output under controlled operating conditions.

2 | Results and Discussion

Figure 1 summarizes the fabrication route of the BM-TENG, including preparation of the leaf-based current collectors, fabrication of the biomimetic triboelectric layers, and final device assembly. Figure 1a shows the fabrication process of the CuNWs-coated microfractals as current collectors for the BM-TENG. A rubber tree leaf skeleton (*Hevea brasiliensis*) was cut to a size of 4 cm × 4 cm and dipped into a CuNWs suspension to make the leaf skeleton conductive. The CuNWs attach to the porous fractal structures of the leaf skeleton because of the capillary forces and form a conformal layer onto their surface [33]. Figure 1b shows the fabrication process of the biomimetic leaf surfaces made from Nylon-6 and PVDF polymers following the same process in our previous research [35]. In this method, a customized electrospinning setup with a metalized leaf-based biotic collector was used for imprinting leaf skeleton architectures into modern polymeric materials. These biomimetic surfaces were directly used as the triboelectric layers for the BM-TENG. Figure 1c depicts

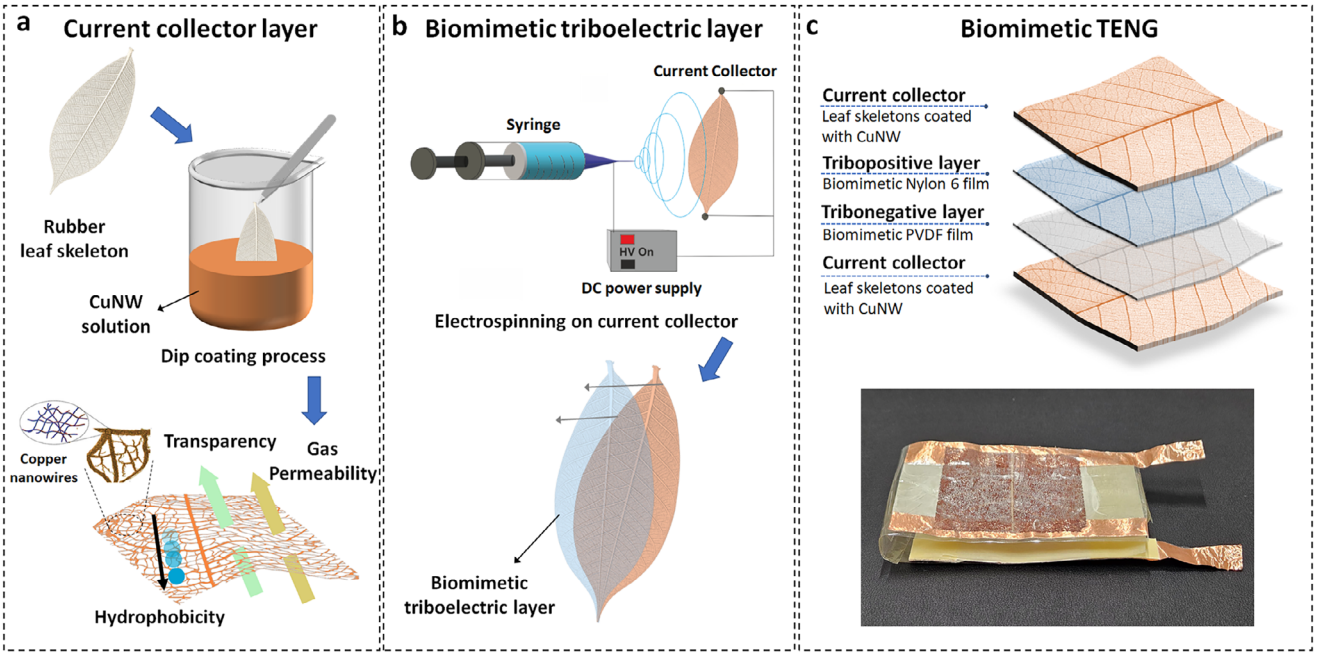

FIGURE 1 | Schematic overview of the fabrication process of the BM-TENG. (a) Fabrication of conductive leaf skeleton as current collectors using dip coating method (b) Fabrication of biomimetic triboelectric layers on top of current collector using customized electrospinning method (c) Schematic of the layers of BM-TENG and digital photograph of the BM-TENG.

the assembly of the BM-TENG, in which the Nylon 6 and PVDF triboelectric layers are separated by an interlayer Tesa 4671 GE tape (made with rayon), while the outer layers of conductive leaf skeletons serve as current collectors. The BM-TENG is further encapsulated with cellulose tape to ensure structural integrity, electrical insulation, and protection of CuNWs from moisture. Figure 1c also shows the digital image of the BM-TENG.

The key design concept is that the leaf skeleton is not only a textured surface but an architected transport network. Its hierarchical veins provide long-range, continuous pathways that can guide conductive nanowires into interconnected routes while maintaining macroscopic porosity for air/moisture transport. Using the same natural template for both the current collector (CuNWs-coated leaf skeleton) and the triboelectric layers (electrospun microfractals in Nylon-6 and PVDF) enables coupled improvements in charge generation and charge collection/transport, while retaining flexibility and breathability.

Figure 2 presents SEM images of the different surfaces used in the BM-TENG. Figure 2a,b show the native rubber leaf skeleton and the CuNWs-coated leaf skeleton, respectively, used as the current collector. The hierarchical leaf-vein microfractal architecture is clearly visible. Importantly, the CuNWs are selectively immobilized along the vein framework, forming conformal conductive pathways while preserving the intrinsic porosity of the leaf skeleton. This results in a guided CuNW network that follows the natural vein topology. The insets in Figure 2a,b show magnified views of the native and CuNWs-coated vein surfaces, respectively. Figure 2c,d show biomimetic triboelectric surfaces replicated from the leaf architecture using Nylon-6 and PVDF, respectively. The replicated structures closely reproduce the original leaf-skeleton geometry, and the insets reveal the underlying nanofiber network in greater detail.

To determine the 2D surface area of the rubber leaf skeleton, a total of ten optical microscope images were analyzed, each acquired with a field of view of approximately 1 mm. Image analysis was performed using ImageJ (Fiji) software. Spatial calibration was established by defining the scale-to-pixel ratio based on the corresponding scale bar provided in each optical image prior to analysis. The images were subsequently converted to binary (black-and-white) grayscale contrast as depicted in Figure S1. The surface area was then quantified from the binary version of the images using the built-in measurement tools in ImageJ (see Table S1), and the calculated values were averaged across all samples. The analysis revealed that the mean effective surface area of the leaf skeleton corresponded to approximately 30.17 ± 1.33% of the total image area, indicating a relatively high density and complex vein network architecture characteristic of the rubber leaf structure. This high areal vein fraction implies a dense, multi-order branching network that can act as a pre-defined conductive "highway system" for nanowire immobilization and long-range percolation. In the context of CuNWs networks, such an architecture is expected to lower the effective percolation threshold by concentrating conductive material into connected pathways rather than distributing it uniformly over a planar area.

To fabricate the current collector for dip coating experiments, leaf skeletons of rubber tree (*H. brasiliensis*) were cut into 5 cm × 3 cm dimensions. Using tweezers, these leaf skeletons were dipped in 40 mL CuNWs solution in ethanol having a concentration of 375 μg mL^{-1}. After dipping, the leaf skeletons were mounted on a 3D frame and placed on a hot plate at 60°C for drying. The edges of the leaf skeletons were mounted to the frame, ensuring that the remaining portions did not come into contact with any surface. This configuration promoted capillary-driven flow of the CuNWs solution during drying, facilitating the deposition and adhesion of CuNWs onto the leaf skeleton

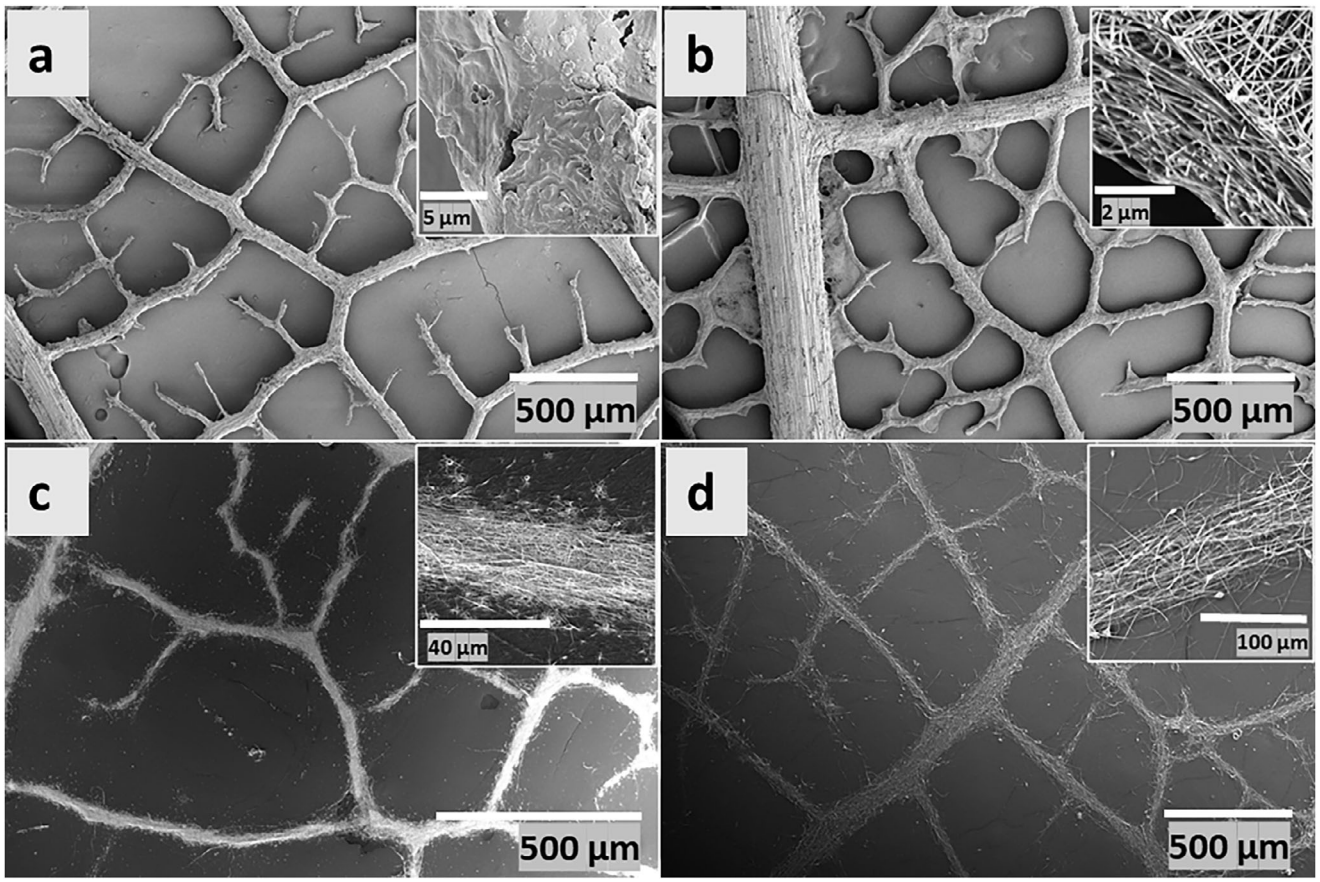

FIGURE 2 | SEM images of the Rubber (*Hevea brasiliensis)* leaf skeleton and biomimetic surface of rubber leaf skeleton. (a) Real leaf skeleton of rubber tree (b) CuNWs-coated conductive rubber leaf skeleton used as current collector layer (c) Biomimetic rubber leaf skeleton surface made with Nylon 6 polymer used as tribopositive layer (d) Biomimetic rubber leaf skeleton surface made with Polyvinylidene Fluoride (PVDF) polymer used as tribonegative layer.

structure depicted in Figure 1a. Once dried, the resistance of the leaf skeletons was measured. The dipping, drying, measurement cycle was repeated multiple times until the resistance was around ~15 Ω sq^{-1}. The weight of the leaf skeleton was noted before and after CuNWs coating cycles to determine the amount of material loaded onto the leaf skeleton. Figure 3a represents the decreasing resistance values with increasing number of dipping cycles. The uniformity of the coating was confirmed by checking multiple sheet resistance values at different locations along the X-Y axis on the conductive leaf skeleton. Figure 3b shows the uniform conductivity mapping of the conductive leaf skeleton surface plotted from sheet resistance measurements. To evaluate the mechanical deformation behavior of the CuNWs-coated conductive leaf skeleton, cyclic bending tests were performed for 1000 cycles under repeated mechanical loading. The evolution of resistance value was continuously monitored throughout the test to assess electrical stability under dynamic bending cycles. The results demonstrate negligible variation in relative resistance over 1000 bending cycles, as shown in Figure 3c, indicating excellent mechanical robustness and electrical reliability of the conductive network. The digital photographs of the CuNWs-coated rubber leaf skeleton and CuNWs-coated PVDF nanofiber surfaces as control planar surface have been depicted in Figure 3d–f, and their corresponding SEM images are shown in Figure 3g–i. SEM images reveal a distinct difference in the morphology of the CuNWs networks depending on the substrate. In the case of the leaf skeleton substrate, bundling of CuNWs is clearly observed, indicating guided alignment and aggregation along the underlying microstructure. In contrast, the CuNWs deposited on the planar substrate form a more randomly distributed mesh network with no evident directional organization.

Conventional TENGs commonly employ metallic foils or conductive films as current collectors because of their low sheet resistance and efficient charge collection. In contrast, the CuNWs-coated leaf skeleton provides a breathable and mechanically compliant alternative while maintaining a sheet resistance (~15 Ω sq^{-1}) comparable to many reported polymer-based conductive current collectors [50–52]. At identical areal CuNWs loading, the biomimetic leaf-skeleton scaffold exhibited more than three orders of magnitude lower sheet resistance than the planar control, highlighting the strong role of architecture-guided nanowire organization in determining macroscopic transport. To make this comparison conservative, the planar control was prepared using vacuum filtration, which is widely regarded as one of the most effective methods for forming uniform nanowire coatings with low sheet resistance on planar substrates. This difference is significant because CuNWs exhibit strong tendencies for agglomeration and junction-limited transport during deposition, which can severely increase resistance on planar surfaces. In contrast, the leaf skeleton promotes guided alignment and local bundling of CuNWs along hierarchical veins, improving inter-nanowire

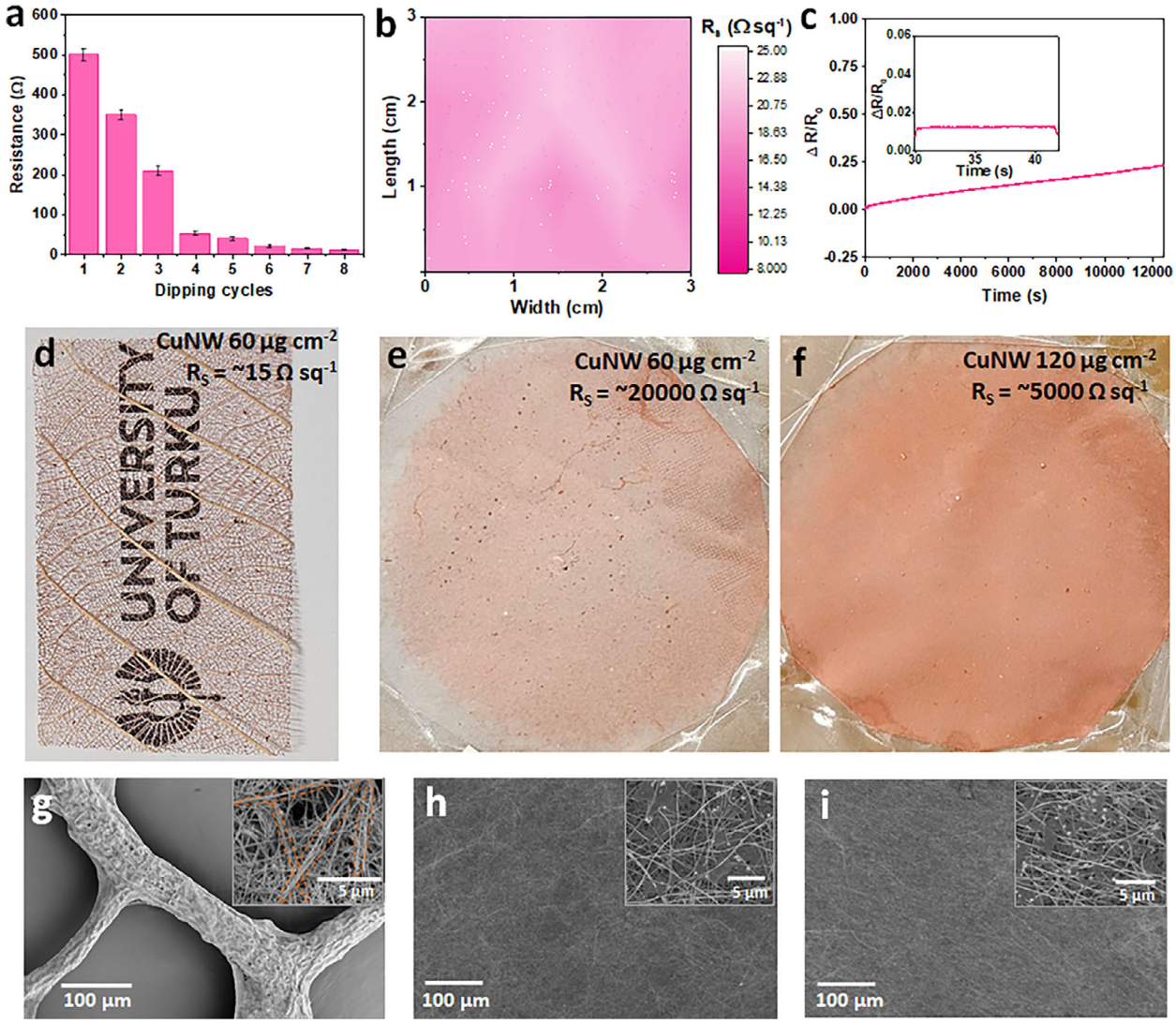

FIGURE 3 | Current collector surface characterization. (a) Histogram showing resistance of the rubber leaf skeleton with respect to the number of dipping cycles. (b) Conductivity mapping showing uniform sheet resistance after CuNWs loading on rubber leaf skeleton surface. (c) Cyclic test of 1000 bending cycles vs relative resistance of the leaf-based current collector at a frequency of 0.083 Hz. Inset shows relative resistance of the biomimetic current collector throughout one full cycle of bending. (d) Digital image of biomimetic current collector loaded with 60 µg cm^{-2} of CuNWs. (e) Digital image of CuNWs coated PVDF nanofiber surface with equal loading quantity of 60 µg cm^{-2} CuNWs. (f) Digital image of CuNWs coated PVDF nanofiber surface with double loading quantity of 120 µg cm^{-2} CuNWs. The sheet resistance, Rs values and the loading concentration of CuNWs are mentioned with the respective digital images in d, e and f. (g) SEM image of CuNWs coated rubber leaf skeleton surface (h) SEM image of CuNWs coated PVDF nanofiber surfaces with equal amount of loading quantity of the rubber leaf. (i) SEM image of CuNWs-coated PVDF nanofiber surfaces with double the loading quantity of the rubber leaf. Inset of each SEM image represents a magnified version of the image in g, h, and i.

connectivity and reducing effective junction resistance [34, 53, 54]. As a result, continuous directional conductive pathways form without complex processing, enabling high conductivity at reduced material loading while preserving macroscopic porosity [31, 55, 56].

Mechanistically, the observed performance gap is consistent with percolation-limited transport in metal nanowire networks, where macroscopic conductivity is primarily governed by long-range connectivity and wire–wire junction quality rather than the intrinsic conductivity of individual nanowires. On planar substrates, randomly oriented CuNWs must exceed a critical areal number density to form a continuous percolated pathway, and the resulting network contains a high density of junctions whose contact resistance can dominate the overall sheet resistance [57]. In contrast, the hierarchical vein architecture of the leaf skeleton acts as a pre-defined conductive scaffold that spatially confines CuNWs along anisotropic pathways, promoting local alignment and bundling. This reduces the number of junctions required to span macroscopic distances, suppresses junction-limited losses, and enables long-range conductive pathways at substantially lower areal mass loading, while leaving large open regions uncoated and preserving breathability [55].

Breathability is an important requirement for wearable and flexible electronics to ensure user comfort, moisture management, and skin compatibility. To quantitatively evaluate the breathability of the BM-TENG, both air permeability and water

vapor transmission rate (WVTR) measurements were performed. Air permeability measurements were conducted using a TESTEX FX 3300-IV Air Permeability Testing Device with a test area of 20 cm^2 under differential pressures ranging from 50 to 500 Pa. The BM-TENG exhibited air permeability values between 30.3 and 267.0 L m^{-2} s^{-1} shown in Figure S4a, demonstrating effective air transport through the porous device structure. In addition, WVTR measurements were carried out according to ASTM F1249 at 23°C and 50% relative humidity. The measurements were performed using an active device area of 2 cm^2, and the results were averaged over three replicate samples. The BM-TENG exhibited an average WVTR value of 56.7 g m^{-2} day^{-1} depicted in Figure S4b, confirming its ability to facilitate moisture transport.

For the breathability measurements, the functional BM-TENG stack, consisting of the biomimetic current collectors, biomimetic triboelectric layers, and separator, was evaluated. The locally applied cellulose tape used for device assembly was not included in the test area, because it served only as an edge-stabilizing component and did not represent the primary active breathable region of the device. This configuration therefore allows the intrinsic air and moisture transport properties of the porous microfractal device architecture to be assessed. In practical device designs, breathable or patterned encapsulation strategies could be incorporated without covering the full active area, thereby preserving air and moisture permeability. To verify that operation of the functional stack is not dependent on the local tape encapsulation, a non-encapsulated BM-TENG was further tested under different tapping forces and subjected to a 5000-cycle durability test. The corresponding results, presented in Figure S5, show comparable electrical output and stable operation without encapsulation.

The simulations are used to provide qualitative mechanistic support for the experimental trend by isolating the intrinsic impact of nanowire directionality and bundling on network sheet resistance under controlled assumptions. The model does not explicitly capture several non-idealities that are prominent in experimental CuNWs coatings, such as time-dependent agglomeration during deposition, partial oxidation, 3D confinement imposed by the substrate microtopography, and spatially heterogeneous junction quality over macroscopic length scales. It is therefore not expected to reproduce the full magnitude of the experimentally observed improvement. Within these defined constraints, theoretical modeling and simulations are employed to systematically evaluate how CuNWs directionality and bundling influence the sheet resistance, R_s of CuNWs networks. First, we examine the impact of directionality in Figure 4f by evaluating the dependence of R_s in directional networks on the standard deviation of the direction angle (σ_Φ). For comparison, Figure 4f also contains the sheet resistance of fully random networks that have no σ_Φ dependence. For $\sigma_\Phi < 10°$, the R_s of directional structures is higher than that of random networks, which we attribute to a low number of contacts. The optimal σ_Φ is found in the 15°–25° range, with a minimum at 22°, which results in a 32% lower sheet resistance in directional networks compared to the fully random structure. Further increase of σ_Φ leads to higher R_s, with directional networks becoming indistinguishable from the random structure for $\sigma_\Phi > 90°$. Next, we assess the impact of bundling in directional networks and report the results in Figure 4g for $\sigma_\Phi = 20°$. The sheet resistance of bundled directional CuNWs networks is plotted against covered area percentage for three different mass densities of 11.3, 33.8, and 61.9 μg cm^{-2}. We observe that bundling decreases the sheet resistance, but only at low mass densities has a significant effect. To further analyze and quantify the impact of directionality and bundling, the difference in percentage Δ between random structures, directional structures, and directional structures bundled to 20% of the area are plotted against CuNWs mass density in Figure 4h. For sub-10 μg cm^{-2} mass density, the impact of bundling is significant and greater than the impact of directionality. However, increasing the mass density beyond 40 μg cm^{-2} reduces the bundling improvement to only 10% (100% vs. 20% covered area in directional networks) and enhances the directionality improvement to 36% (random vs. directional at 100% area covered). Consequently, bundled directional structures have 43% lower sheet resistance than random unbundled networks. Accordingly, we confirm that conductivity is significantly enhanced by the directionality and bundling present in the leaf skeleton-based CuNWs structures investigated in this work.

Unlike copper nanoparticle-based conductive inks, which typically require post-deposition sintering to remove surface ligands and reduce interparticle resistance, the present microfractal architecture enables immediate conductivity enhancement through nanowire bundling. In nanoparticle systems, electrical transport is often limited by high junction resistance and surface oxidation, requiring thermal or photonic sintering treatments that increase processing complexity and are often incompatible with flexible substrates [56, 58]. In contrast, the leaf-inspired vascular network guides CuNWs into locally bundled and partially aligned pathways along the hierarchical venation structure. This geometric confinement significantly reduces the number of nanowire-nanowire junctions and lowers transport resistance without any post-treatment. As a result, a rapid decrease in sheet resistance is achieved, highlighting a key advantage of nanowire-based hierarchical architectures over conventional nanoparticle inks.

Although both simulation and experiment show the same qualitative trend, the experimentally observed advantage of the biomimetic architecture is substantially larger than the approximately threefold improvement predicted by the model. This difference is reasonable because the simulation does not explicitly capture several non-idealities that strongly affect real CuNW coatings, including deposition-induced agglomeration, heterogeneous junction quality, partial oxidation, and long-range connectivity across macroscopic distances. Under these realistic conditions, the guided and bundled transport pathways of the leaf skeleton provide a greater practical benefit than is predicted by the idealized model.

Another key component of the BM-TENG is the biomimetic triboelectric layer: electrospun nanofiber mats that inherit the leaf-skeleton microfractal geometry, thereby introducing hierarchical roughness and compliant microstructures across multiple length scales. Such multiscale topography is expected to increase the real contact area under a given normal force and to create a larger number of localized microcontacts, which elevates triboelectric charge generation during contact electrification. In addition, the interconnected micro–nano features can promote spatially

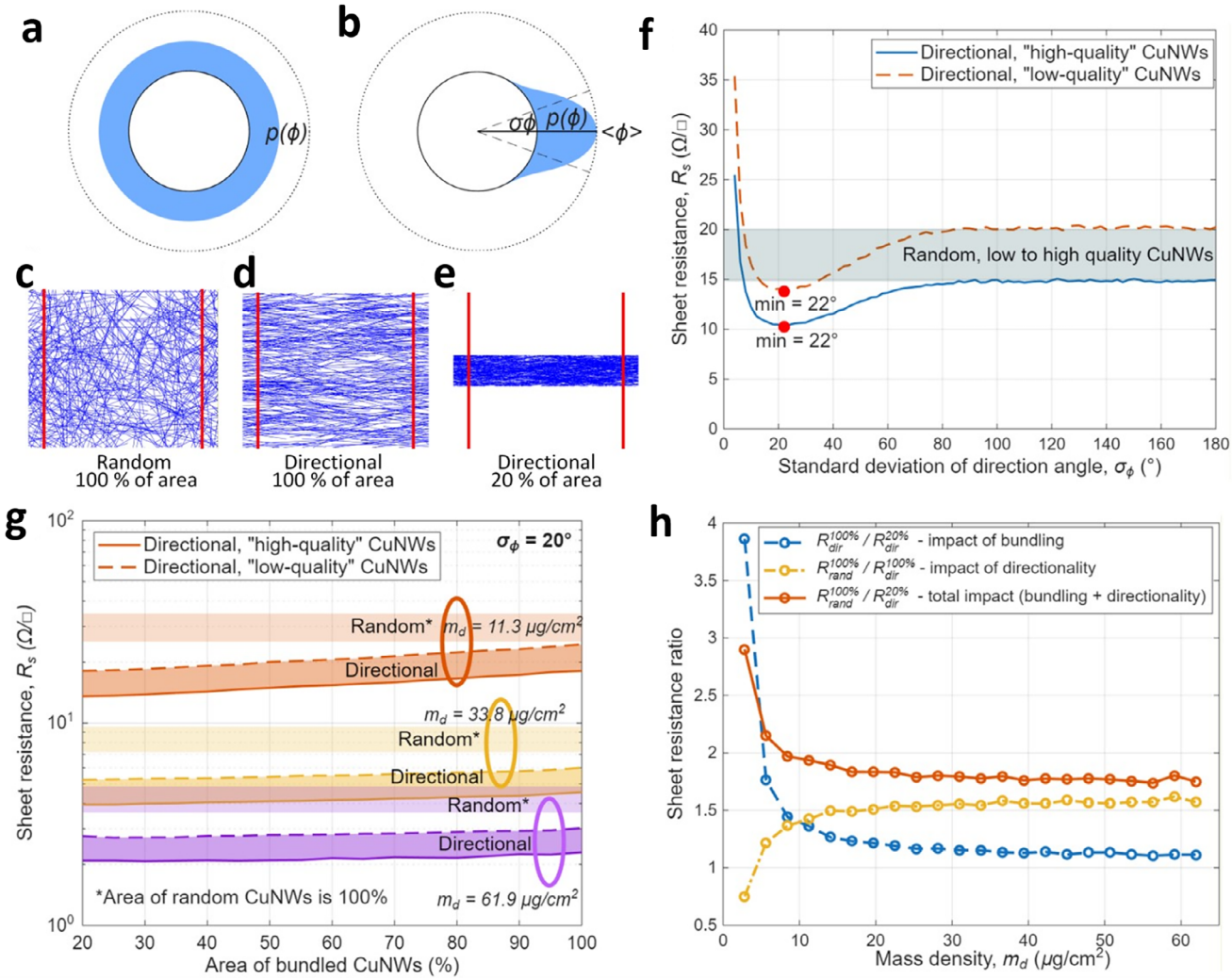

FIGURE 4 | Simulation study of sheet resistance in CuNWs networks interfaced with planar surfaces (random network of CuNWs) and biomimetic surfaces (directional network of CuNWs). Depiction of (a) Random network angle probability $p(\Phi)$, which is the same for all angles, and (b) Directional network defined by mean direction angle $<\Phi>$ and standard deviation of direction angle σ_Φ. CuNWs networks with (c) Random structure, (d) Directional structure, and (e) Bundled directional structure at 20% area. (f) Impact of standard deviation of direction angle σ_Φ on sheet resistance. (g) Impact of bundling area on sheet resistance. (h) Influence of mass density on the impact of bundling and directionality.

distributed charge storage and reduce local charge saturation by offering multiple charge trapping/holding sites. Consequently, for an identical projected footprint area, the replicated microfractals are expected to yield higher transferred charge per cycle and stronger electrostatic induction compared with planar nanofiber layers. Efficient charge transport in the BM-TENG is further enabled by its hierarchical conductive network [34]. In this architecture, local charges generated at the triboelectric interface are rapidly collected and transported through hierarchical interconnected long-range pathways, minimizing charge trapping and resistive losses. The fractal conductive network provides multiple parallel charge transport routes, ensuring stable electrical output even under repeated bending and mechanical deformation.

The electrical output performance of the leaf skeleton-based BM-TENG was systematically investigated under controlled mechanical pressure to evaluate the energy harvesting capability. The device was characterized in terms of open-circuit voltage V_{OC}, short-circuit current I_{SC}, current density, J_{SC} and power density, P_d. The device was also demonstrated in practical applications, including capacitor charging and LED illumination, using energy harvested from human motion. To understand the role of the biomimetic current collector and biomimetic triboelectric layer, the performance of the BM-TENG was compared with three control devices having different layer combinations. Control Device 1 consisted of planar current collectors and planar triboelectric layers, Control Device 2 consisted of planar current collectors and biomimetic triboelectric layers, and Control Device 3 consisted of biomimetic current collectors and planar triboelectric layers. The electrical performances of these devices were evaluated under identical testing conditions.

The electrical response of the BM-TENG was examined under different contact pressures ranging from 20 kPa to 2.5 MPa. The applied pressure was calculated from the force given by the force sensor and the contact area of the cylindrical tapping probe. A cylindrical probe with a diameter of 20 mm was used for all measurements. Figure 5a shows the schematic diagram of the test

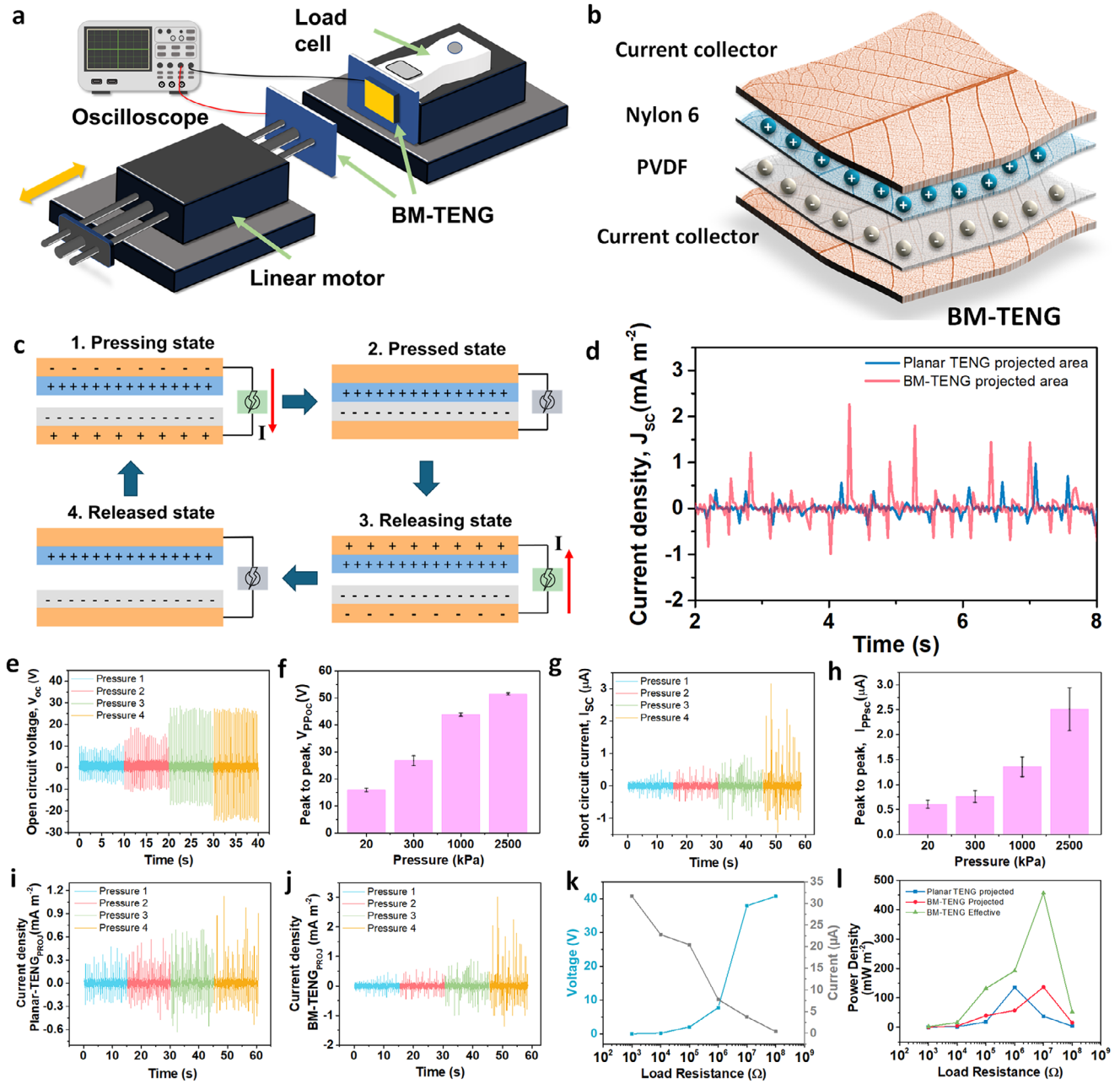

FIGURE 5 | Electrical characterization of the BM-TENG. (a) Representative schematic diagram of the test setup. (b) Schematic of the BM-TENG layers highlighting positive and negative charges of the biomimetic triboelectric layers. (c) Typical mechanism of the BM-TENG. (d) Current density comparison between planar TENG and the BM-TENG considering projected area. (e) Open-circuit voltage, V_{OC} measurement of BM-TENG at different pressures. (f) Histogram plot of mean peak-to- peak V_{OC}. Error bars represent the standard deviation. (g) Short-circuit current I_{SC} measurement of BM-TENG at different pressures. (h) Histogram plot of mean peak-to-peak I_{SC}. Error bars represent the standard deviation. (i) Current density of the planar control TENG considering projected area. (j) Current density of the BM-TENG considering projected area. (k) Current and voltage measurement for BM-TENG with respect to different load values from 1 kΩ to 100 MΩ. (i) Power density calculation of the planar control TENG with projected area, BM-TENG with projected area, and BM-TENG with effective surface area of leaf skeleton processed by ImageJ. Here, Pressure 1 = 20 kPa, Pressure 2 = 300 kPa, Pressure 3 = 1 MPa and Pressure 4 = 2.5 MPa.

setup for the characterization, having a linear motor interfaced with the force sensor to apply repeated mechanical force on the BM-TENG, and the electrical contacts of the BM-TENG connected to a digital oscilloscope to measure the corresponding open-circuit voltage generated. Figure 5b shows the BM-TENG layout having positive and negative charge on the triboelectric layers, and Figure 5c shows the overall charge generation mechanism of the BM-TENG in general due to contact and separation cycles. The output voltages and current waveforms for the BM-TENG under varying forces are shown in Figure 5e,g, and their corresponding histograms are shown in Figure 5f,h, where the values of the histograms represent the average value of the peak-to-peak voltages and currents at each different pressure, and the error bars represent the standard deviation values.

The highest ten tapping measurements at each applied pressure condition were used to choose the average peak of the histogram. The reported values represent the mean ± standard deviation calculated from these repeated measurements. The BM-TENG achieved a maximum open-circuit voltage of ~52 V peak-to-peak, whereas the planar Control Device 1 produced a maximum voltage of only ~26 V. Similarly, the BM-TENG generated a maximum short-circuit current of ~3.2 μA, compared to ~1.23 μA for the planar control device. The open-circuit voltage and short-circuit current outputs of all control devices are presented in Figure S6 and Figure S7, respectively, and comparison of their electrical performance is provided in Table S2. With increasing force, all the devices exhibited higher power generation, which correlates with the typical nature commonly observed in TENG devices. Both the open-circuit voltage and short-circuit current increased with applied pressure, which is consistent with improved real contact area and more efficient charge transfer between the triboelectric layers during each contact–separation cycle. The approximately linear dependence of the output on pressure indicates stable mechanical-to-electrical conversion within the investigated force range.

In addition, the flexible leaf skeleton structure allows localized deformation along the vein network, further amplifying microscale contact points and facilitating charge generation. This advantage of the fractal geometry becomes evident when the electrical performance of the BM-TENG is compared with the three control devices, as summarized in Table S2. Using the projected device area as the primary normalization basis, the BM-TENG exhibited a current density of ~3 mA m^{-2}, which is significantly higher than the ~1.13 mA m^{-2} obtained for the planar control. When the effective material area is considered as a secondary normalization metric, the current density of the BM-TENG increases to ~10 mA m^{-2}, indicating more efficient charge generation and charge collection within the biomimetic fractal architecture. The transferred charge per cycle for the BM-TENG was calculated to be 67.24 nC, whereas the planar TENG gave a lower value of 27.35 nC. The increase in current density arises because the porous leaf skeleton structure covers only ~30% of the effective 2D area compared to the continuous planar surface. As a result, the generated current is distributed over a smaller effective area with higher material density, leading to a higher current density when normalized by area. The overall current density of the planar TENG and the BM-TENG under different pressures is shown in Figure 5i,j. The current density, J_{SC}, was calculated by normalizing the measured short-circuit current to the device area:

$$J_{sc} = \frac{I_{sc}}{A} \tag{1}$$

where I_{SC} is the measured current and A is the active area of the device.

In conventional TENG studies, the electrical output densities are typically normalized by the projected contact area of the device, which enables direct comparison across different reports. Following this common practice, the present BM-TENG device has a nominal projected area of 10.5 cm^2, based on its physical dimensions of 3.5 cm × 3 cm. However, due to the inherently porous architecture of the leaf skeleton, only a portion of this apparent area consists of solid vein structures that can physically participate in contact electrification. ImageJ-based image analysis, as described in the previous section (refer to Figure S1), revealed that the leaf veins occupy approximately 30% of the projected area, corresponding to the actual material coverage available for triboelectric interaction. This indicates that the true solid–solid contact region is substantially smaller than the apparent device footprint. While the projected area remains the standard metric for reporting device-level performance, evaluating the output relative to the effective leaf coverage provides additional insight into the material-level charge generation efficiency.

The improved electrical output also results in a noticeable increase in power density. Figure 5k depicts the voltage and current outputs for the BM-TENG under different load resistances ranging from 1 kΩ to 100 MΩ. The instantaneous electrical power generated by the device can be expressed as

$$P = VI \tag{2}$$

where V and I represent the output voltage and current, respectively, under a particular load resistance. The maximum power output was determined under the maximum applied pressure condition, which is 2.5 MPa, since higher applied pressure generated the highest electrical output response from the BM-TENG device. At the fixed pressure, ten tapping cycles were considered for each external load resistance, and the average voltage was calculated. The current was determined using Ohm's law,

$$I = \frac{V}{R} \tag{3}$$

and the instantaneous power was calculated using $P = VI$. The highest calculated power value obtained at a specific load resistance, in this case at 10 MΩ for the BM-TENG, was considered as the maximum power output of the device. When normalized to the device area, the power density is given by

$$P_d = \frac{VI}{A} \tag{4}$$

Based on the planar area, the control TENG achieves a maximum power density of ~135.80 mW m^{-2} at an optimal load resistance. In comparison, the BM-TENG achieved a maximum power density of ~136.91 mW m^{-2} for projected area normalization and ~456.35 mW m^{-2} for effective material area normalization, as shown in Figure 5l, highlighting the strong contribution of the porous microfractal architecture. The power density curves of all four devices are depicted in Figure S9. This enhancement is attributed primarily to the efficient conductive network and the hierarchical microstructured interface of the BM-TENG. In addition, normalization to the effective leaf-covered area further highlights the intrinsic output per active material area. This perspective highlights the intrinsic advantage of the biomimetic vein network, where localized microstructured features can yield substantial triboelectric output despite limited material coverage. Such analysis does not replace conventional normalization but rather complements it by revealing how natural hierarchical structures can enhance charge generation efficiency per unit active material area. A direct comparison between the planar TENG and the BM-TENG is summarized in Table S3. A broader

comparison with recently reported flexible, bioinspired, and breathable triboelectric nanogenerators is provided in Table S4, demonstrating the competitive performance of the present BM-TENG.

The frequency-dependent electrical behaviour of the BM-TENG was investigated over a frequency range of 0.5–2 Hz with an interval of 0.5 Hz. As shown in Figure S2a, the open-circuit voltage waveforms exhibit consistent peak amplitudes across different frequencies, while the number of voltage pulses increases with frequency over a certain period of time. This indicates that the maximum achievable surface charge density is independent of frequency, provided that sufficient contact time is maintained during each cycle. In contrast, the short-circuit current shows a clear increase with operating frequency (see Figure S2b). This behaviour can be attributed to the current expression:

$$I = \frac{dQ}{dt} \tag{5}$$

where Q is the transferred charge per cycle. At higher frequencies, the time interval (dt) between each contact separation events decreases, leading to a higher rate of charge transfer even when the total transferred charge per cycle remains constant. In this manner, the current output increases with frequency.

To evaluate the mechanical flexibility of the BM-TENG, the device was bent using mechanical grippers mounted on a linear translation stage, and the corresponding electrical response was recorded. Figure S10 shows the applied curvature values and their corresponding open-circuit voltage outputs. The histogram plot demonstrates that the electrical output increases with increasing curvature, with the full BM-TENG generating an open-circuit voltage of up to 5 V peak-to-peak at a maximum curvature of 125 m^{-1}. These results confirm that the BM-TENG can maintain stable electrical performance under mechanical deformation, highlighting its suitability for flexible and wearable applications.

Figure 6a represents the overview of the BM-TENG application, self- and low-powered electronics containing mechanical excitation on the BM-TENG, followed by an energy harvesting unit and powering the electronics. To check the reliability, the BM-TENG was put to cyclic testing for ~10 000 cycles of repeated mechanical tapping with 1 MPa at a frequency of 5.45 Hz. The BM-TENG showed a similar waveform for ~10 000 cycles, having peak-to-peak voltage around 50 V with a very low amount of deviation as depicted in Figure 6b. This confirms the reliability of the device to perform consistently over time for repeated usage. The output voltage and current of the BM-TENG were further examined under different finger-tapping pressures, and the corresponding voltage and current responses are presented in Figure S3. To illustrate its capability for powering low-power electronic devices, the BM-TENG was directly connected to 20 light-emitting diodes (LEDs) connected in series to form a UTU (University of Turku) logo. With each finger tap, the LEDs were successfully illuminated, as shown in Figure 6c, highlighting the high impulsive voltage output and practical energy harvesting potential of the BM-TENG. The real-time LED illumination process is further demonstrated in Video S1. The applicability of the BM-TENG to store energy was further demonstrated by charging capacitors with different capacitance values, as shown in Figure 6d,e. The charging profiles exhibit a clear dependence on capacitance, with smaller capacitors charging more rapidly and achieving higher voltages within a shorter time. For a given amount of transferred charge per cycle, a smaller capacitance results in a larger voltage increase. The stable and repeatable charging-discharging cycles help the BM-TENG to serve as a reliable power source for low-power electronics, such as calculators and LEDs, after appropriate energy storage.

To demonstrate the capability of the BM-TENG to harvest energy from human motion and ambient mechanical vibrations, the device was directly attached to the human wrist and elbow. Periodic bending and movement of the wrist and elbow induced contact-separation processes within the BM-TENG, generating distinct voltage signals that enabled both motion detection and electrical energy generation, as shown in Figure 6f,g. The real-time voltage generation during wrist and elbow movements is further demonstrated in Videos S2 and S3, respectively. These results confirm the effectiveness of the BM-TENG in converting natural human body movements into usable electrical output. The practical applicability of the BM-TENG was further demonstrated by mounting the device onto a wall-mounted light switch, where repeated tapping produced a peak output voltage of approximately 4 V. Similarly, when subjected to foot tapping, the BM-TENG generated voltage peaks of up to ~2 V, indicating stable energy harvesting under different modes of mechanical excitation. These demonstrations were depicted in Figure 6h,i.

The BM-TENG was also demonstrated as a self-powered sensor for robotic gripper monitoring. In this application, the BM-TENG was attached to a robotic gripper to detect grasping and releasing events. When the gripper grasped an object, the applied mechanical deformation generated a positive voltage spike, whereas releasing the object produced a negative voltage spike. These distinct signal responses enabled clear differentiation between gripping and releasing actions. The corresponding voltage signals and their analysis are presented in Figure 6k and Video S4, demonstrating the potential of the BM-TENG as a self-powered sensing interface for robotic and automation applications.

The BM-TENG was also demonstrated as a wireless signal-transmission platform, making it a promising candidate for integration into wireless communication systems. To demonstrate the practical applicability of the BM-TENG in real-world wireless transmission circuits, the generated voltage signals were processed using a bridge rectifier, a comparator circuit, and an Arduino Nano BLE module to wirelessly transmit signals or encoded messages to a mobile phone application via Bluetooth communication. For wearable health-monitoring applications, the BM-TENG was placed on a surgical mask to monitor human breathing activity. During inhalation, the airflow mechanically excites the BM-TENG, generating a characteristic burst of voltage signals that appears as a distinct high-activity window. During exhalation, the signal returns to its baseline level. Consequently, each breathing cycle can be identified from the appearance and disappearance of these voltage-activity windows. To improve signal consistency, the BM-TENG output was rectified using a full-bridge rectifier to convert the alternating output into a single-polarity signal. The rectified signal was then directly processed

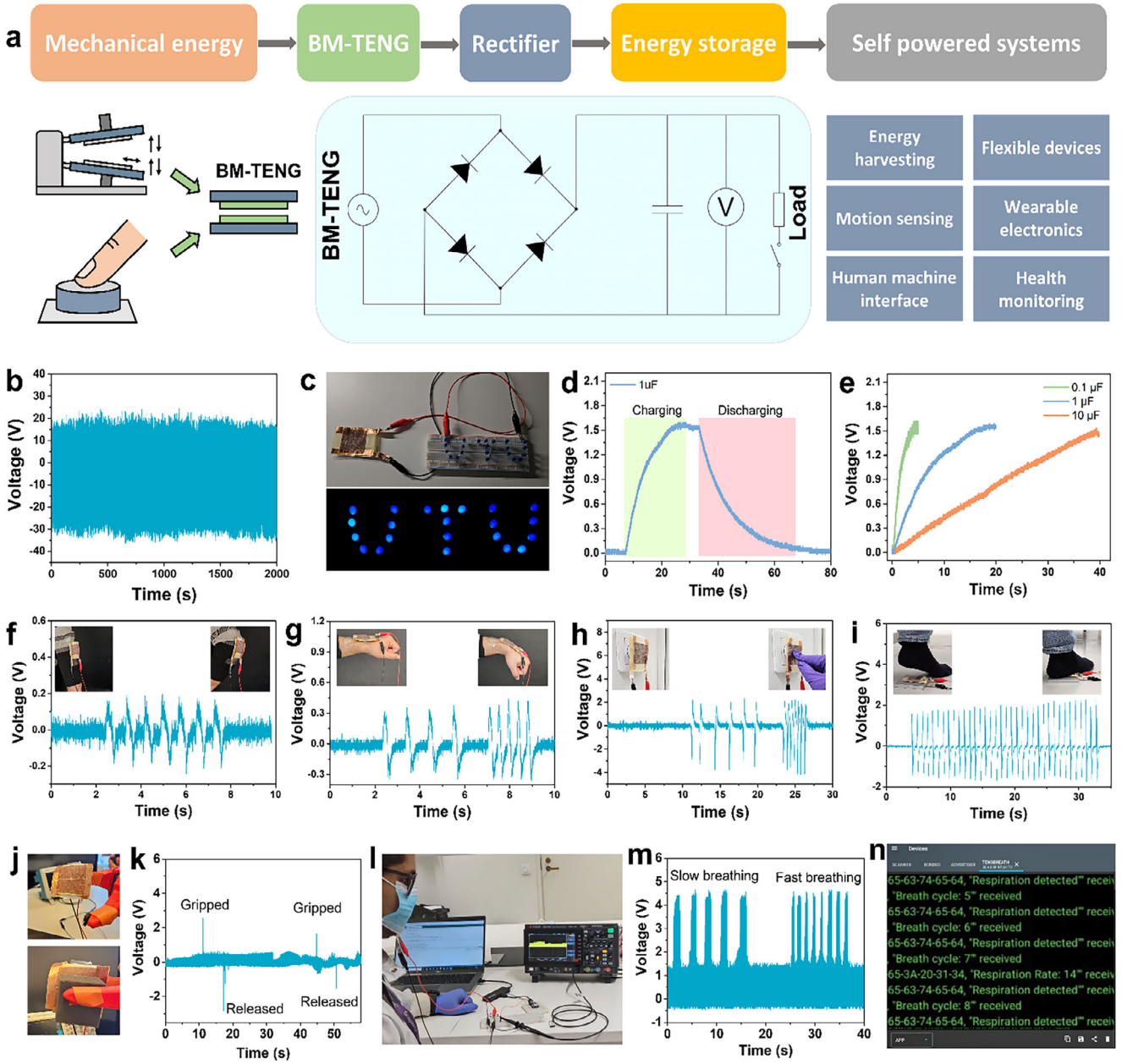

FIGURE 6 | Application and demonstration experiments of the BM-TENG. (a) Schematic of current and potential applications of the BM-TENG. (b) Cyclic voltage measurement test with repeated tapping at 5.45 Hz frequency and 1 MPa pressure for ~10000 cycles. (c) Lighting up 22 LEDs making a University of Turku (UTU) logo with simultaneous tapping cycles. (d) Charging and discharging rate of a 1 μF capacitor with tapping cycles. (e) Charging rate of different capacitors of capacitance values 0.1, 1, and 10 μF. (f) BM-TENG attached to the elbow showing voltage output during elbow motion. (g) BM-TENG attached to the wrist showing voltage output during periodic wrist bending. (h) BM-TENG mounted on a wall switch showing voltage output under repeated tapping. (i) Voltage output under foot-tapping excitation. (j) Digital photographs of the BM-TENG attached to a robotic gripper for grip sensing. Upper image shows the BM-TENG integrated onto the robotic gripper, while the lower image shows the gripper holding an object during the sensing operation. (k) Signal response of the gripping and releasing cycles visualized through a digital oscilloscope. (l) Digital photograph of the breath monitoring setup and demonstration. (m) Signal response of the breathing cycles visualized through a digital oscilloscope. (n) Notification of breath cycle detection and BPM value in an Android-based mobile application connected via Bluetooth.

using a custom-programmed Arduino Nano BLE microcontroller, which converted the detected breathing events into digital messages for wireless transmission to a mobile application via Bluetooth. The transmitted data were monitored on a smartphone using the nRF Connect application. Figure 6m shows representative breathing-monitoring signals, clearly distinguishing slow and fast breathing patterns, where faster breathing produces more frequent voltage-activity windows. The corresponding breathing-per-minute (BPM) rate was displayed on the Android application interface as depicted in Figure 6n. The demonstration of the breath monitoring is further demonstrated in the Video S5.

In addition, the BM-TENG was further demonstrated as a self-powered human-machine interface for wireless Morse-code

-based communication. In this demonstration, the BM-TENG output was first rectified using a bridge rectifier and then processed through a comparator circuit and an Arduino Nano BLE module. The microcontroller program was specifically designed to identify different tapping time intervals as Morse-code inputs. When two voltage spikes were detected within a time interval shorter than 300 ms, the input was identified as a "dot" signal. In contrast, voltage spikes separated by a time interval between 300 ms and 1500 ms were interpreted as a "dash" signal. These different time intervals were generated through fast and slow manual tapping of the BM-TENG device, respectively, as demonstrated in Video S6. Figure S11 presents the signal analysis corresponding to Morse-code-based generation of a "HELP" emergency message using BM-TENG tapping inputs.'

It is noteworthy to mention that the present BM-TENG is not intended to be presented as a fully sustainable device, as it still incorporates conventional triboelectric polymers, including Nylon-6 and PVDF, DMF-assisted PVDF processing, and Cu-based conductive networks. Rather, the sustainability aspect of this work arises from the resource-efficient design strategy enabled by the biomimetic microfractal architecture. Specifically, the leaf-skeleton-derived hierarchical network allows high electrical output to be achieved at reduced CuNW loading, replaces commonly used noble-metal nanowires such as AgNWs with a more abundant and cost-effective Cu-based alternative, and maintains breathability through its intrinsically porous architecture. Therefore, the bioinspired design should be viewed as an architecture-guided, material-efficient step toward more sustainable flexible TENG platforms. Future efforts should focus on further improving the environmental profile of such devices by replacing PVDF and Nylon-6 with biodegradable or bio-derived triboelectric polymers and by developing greener solvent-processing routes [59–61].

3 | Conclusions

In summary, we report a biomimetic microfractal triboelectric nanogenerator based on leaf-skeleton vascular architectures for breathable and flexible energy harvesting. The leaf skeleton functions both as a porous current-collector scaffold for guided and locally bundled CuNWs pathways and as a template for replicating hierarchical microfractals into the triboelectric layers. This design enabled a low sheet resistance of ~15 Ω sq^{-1} and more than three orders of magnitude lower sheet resistance than the planar control under identical CuNWs loading conditions. Supported by qualitative resistor-network simulations, the results highlight the roles of directionality and bundling in reducing transport losses and improving device performance under realistic conditions. The BM-TENG achieved a maximum power density of 136.91 mW m^{-2} with a projected area and 456.35 mW m^{-2} with effective material area, compared to 135.80 mW m^{-2} over the planar control while using 50% lower CuNWs loading, and maintained stable output over ~10 000 cycles. Together with capacitor charging, LED illumination, and human-motion energy harvesting demonstrations, these results establish leaf-inspired microfractal architectures as a scalable and material-efficient route toward breathable triboelectric energy harvesters, while further improvements in polymer selection and solvent processing will be required to realize fully sustainable devices.

4 | Methods

4.1 | Materials

To prepare electrospun nanofibers, Nylon 6 (N-6) and Polyvinylidene fluoride (PVDF) were purchased from Sigma-Aldrich. To encapsulate the BM-TENG, cellulose tape was purchased from 3 M. For the separation layer, Tesa 4671 GE tape (made with rayon) was purchased from Finland. Connecting wires were purchased from Farnell to fabricate electrical contacts of the BM-TENG. Solvents like dimethylformamide (DMF), acetone, and formic acid used during the experiments were purchased from Sigma-Aldrich. Rubber leaf skeletons used in the experiments were purchased from "Leaf Vein Crafts", Toronto, Canada.

4.2 | Synthesis of CuNWs

CuNWs were synthesized according to a previously reported procedure with some modification [62]. Briefly, $CuCl_2{\cdot}2H_2O$ (85 mg, 0.5 mmol), glucose (207.5 mg, 1.05 mmol), hexadecylamine (HDA, 665 mg, 2.25 mmol), and reverse osmosis water (40 mL) were added to a glass beaker and stirred vigorously at room temperature for 5 h to form a homogeneous solution. The mixture was then transferred to a 200 mL Teflon-lined stainless-steel autoclave, sealed, and heated at 110°C for 12 h without further agitation. The CuNWs were purified through three cycles of centrifugation (6000 rpm, 5 min) and redispersion in ethanol to remove synthesis byproducts. A fourth wash was done using a propionic acid and ethanol solution (1:29) to remove remaining surface residues, followed by two final ethanol rinses. The purified CuNWs were then dispersed in 40 mL of ethanol for characterization and film fabrication. This stock solution had a concentration of 0.75 mg/mL.

4.3 | Electrospinning of the Triboelectric Layers

Electrospinning was performed to produce Nylon 6 and PVDF nanofiber-based biomimetic surfaces. The electrospinning setup was modified by replacing the metallic plate collector with a biotic collector as shown in our previous studies [63]. CuNWs-coated rubber leaf (current collector), fabricated using the dip coating method, was used directly as the negative collector, which acts as a surface template. Due to the microfractal structure of the leaf skeleton, the nanofibers mostly deposited onto the surface of the leaf-based current collector, replicating similar architectures. For electrospinning Nylon 6 nanofibers, a 22 wt.% Nylon 6 solution was prepared by dissolving Nylon 6 in formic acid. The solution was sonicated for 1 h at room temperature. The polymer solution was inserted into a 10 mL syringe. 17 kV of positive voltage was applied at a flow rate of 1 μL/min. A distance of 12–14 cm was fixed between the syringe needle and the collector throughout the electrospinning process for Nylon 6 fibers. For electrospinning PVDF nanofibers, a 15 wt.% PVDF solution was prepared by dissolving PVDF in Acetone and DMF with a ratio of 4:6. The solution was stirred with a magnetic stirrer at 250 rpm for 24 hr at 50°C. The polymer solution was inserted in a 10 mL syringe connected to the syringe pump. 17 kV of positive voltage was applied having a flow rate of 10 μL min^{-1}. A distance of 15–16 cm was maintained between the syringe needle and the

collector throughout the electrospinning process for PVDF fibers. The deposited nanofibers, along with the CuNWs-coated current collector, act as an electrode for the BM-TENG.

4.4 | Fabrication of Flexible BM-TENG

The fabrication of the BM-TENG involved multiple steps to ensure optimal performance. CuNWs-coated leaf skeletons were utilized as current collectors due to their high conductivity and bioinspired structure. The triboelectric layers were composed of biomimetic electrospun surfaces, with Nylon 6 as the tribopositive material and PVDF serving as the tribonegative counterpart. These materials were chosen for their excellent triboelectric properties and mechanical flexibility. Tesa 4671 GE tape was employed as a separator to maintain consistent spacing between the triboelectric layers, enhancing charge transfer efficiency. The entire structure was encapsulated using adhesive cellulose tape to provide mechanical stability and environmental protection. Electrical connections were established using copper tape, ensuring reliable charge collection and transfer. The integration of these materials and structural components resulted in a flexible BM-TENG, suitable for sustainable energy harvesting applications. Similarly, for comparison purposes, three control TENG devices were fabricated to systematically evaluate the individual contributions of the conductive current collector architecture and the triboelectric surface morphology. Control Device 1 consisted of planar CuNW-coated conductive PVDF films as the current collector layers and electrospun Nylon-6 and PVDF nanofiber mats deposited on planar aluminum foil substrates as the triboelectric layers. Control Device 2 consisted of planar CuNW-coated conductive PVDF current collectors combined with biomimetic Nylon-6 and PVDF triboelectric layers replicated from the leaf-skeleton architecture. Control Device 3 consisted of CuNW-coated leaf-skeleton current collectors combined with planar Nylon-6 and PVDF triboelectric layers deposited on planar aluminum foil substrates. For all control devices, the same Tesa 4671 GE tape was used as the separator layer to maintain a consistent gap spacing between the triboelectric surfaces.

4.5 | Characterization

The electrospun biomimetic nanofiber surfaces were produced using an electrospinning setup (Spinbox by Bioinicia, Spain). High-resolution surface analysis of leaf skeleton and biomimetic surfaces was performed using a Scanning Electron Microscope (SEM) (Thermo Scientific Inc., Eindhoven, The Netherlands) at 2 kV with an operating current of 25 pA. Electrical characterization of the BM-TENG was performed using a combined interface of a linear actuator (FESTO ELGT BS 90-100-20P), load cell (FX29K0-040B-0025-L), a digital oscilloscope (KEYSIGHT DSOX1204G), and a source meter (Keithley 2400). The relative change in voltage level produced by the BM-TENG was measured using the digital oscilloscope. To measure the open-circuit voltage V_{OC} and short-circuit current I_{SC}, the probe positive and negative ends were directly connected to both the electrical contacts of the BM-TENG. Sheet resistance measurements were carried out using an Ossila four-point probe system. To account for the spatial irregularity of the porous microfractal scaffold, measurements were collected from five different locations across the conductive network, and the average value was reported. Soft-tipped probes with rounded tips (radius: 0.24 mm) were used during the measurements to minimize potential damage to the delicate conductive networks on the leaf skeleton and PVDF nanofibers. The demonstration experiments involved one of the authors as the participant. The participant voluntarily took part in the study and provided informed consent for participation and publication of any related images or data presented in this manuscript.

4.6 | CuNW Network Simulation and Modelling

CuNWs networks were constructed using individual nanowires, each defined by length (100 μm), diameter (100 nm), randomly selected initial coordinates, positional direction angle with respect to the *x*-axis (Φ), and CuNWs quality in terms of carrier transport as determined by resistivity model parameters. The resistivity of each CuNW is modeled to account for the two dominant mechanisms, i.e., surface scattering and the grain boundary effect [64]. The Fuchs-Sondheimer model [65] is used to describe surface scattering through partial specular reflection at the wire surfaces, characterized by the specularity parameter (p), while the Mayadas-Shatzkes model [66] accounts for the grain boundary scattering defined by the reflection coefficient (R), which quantifies carrier backscattering at grain interfaces along the wire length. The range of meaningful p and R values is limited; therefore, we designate two edge cases as "high-quality" CuNWs ($p = 0.6$, $R = 0.1$) and "low-quality" CuNWs ($p = 0.1$, $R = 0.5$), each corresponding to realistic low and high resistivity. The CuNWs networks are defined by mass density, area of bundled CuNWs, and by the direction angle probability $p(\Phi)$. We analyzed networks with either a randomly oriented angle probability (Figure 4a) or a directional distribution with a Gaussian profile, as shown in Figure 4b, defined by the mean ($<\Phi> = 0$) and the standard deviation of the direction angle (σ_Φ). For contacts or junctions between CuNWs, only 20% of them (selected randomly) are considered "good contacts" with contact resistance set to 200 Ω. Other junctions are designated as "bad contacts" with contact resistance set to 1 MΩ. Our approach allows us to assess in detail the effects of directionality and bundling of CuNWs on the overall sheet resistance (R_s) of CuNWs networks, with basic networks illustrated in Figure 4c–e. The CuNWs network simulator was implemented in MATLAB. Each nanowire is discretized into sub-segments, forming equivalent resistors between each pair of adjacent junctions, and the resulting resistor network is solved using Kirchhoff's laws. Due to the stochastic nature of network generation, 100 samples are generated for each configuration (> 20000 samples simulated), and the reported results represent their average values.

4.7 | Breathability Measurements

Air permeability and water vapor transmission rate (WVTR) measurements were performed to quantitatively evaluate the breathability of the BM-TENG. For these measurements, the functional BM-TENG stack, including the biomimetic current collectors, biomimetic triboelectric layers, and separator, was tested without the cellulose-tape encapsulation layer. Air permeability was measured using a TESTEX FX 3300-IV Air Permeability Testing Device with a test area of 20 cm^2. Measurements were

conducted under differential pressures ranging from 50 to 500 Pa. WVTR measurements were performed using a Labthink C303H Water Vapor Transmission Rate Test System according to ASTM F1249 at 23°C and 50% relative humidity. The active test area was 2 cm^2, and the reported WVTR value represents the average of three replicate samples. All the breathability measurements were conducted by Measurlabs (Measur Oy), Helsinki, Finland.

Author Contributions

A.B.–Writing the original draft, BM-TENG fabrication, electrical characterization, demonstrations, formal analysis, and reviewing. M.M.–Simulation studies, methodology, reviewing and editing. A.P.–Material synthesis, device fabrication and characterization. R.G.–SEM imaging, material synthesis, assistance in fabrication. A.Ku.–Material synthesis and demonstration experiments. M.P.–Simulation studies, investigation, reviewing, and editing. A.Ko.–Project discussion, demonstration experiments, reviewing and editing. V.S.–Conceived the idea, guidance, funding acquisition, resources, writing the draft, reviewing & editing.

Acknowledgements

This work was supported by the Research Council of Finland through the DURATRANS project (Grant Number 364408, 2024–2027) under the M-ERA.Net framework. The authors are thankful to the Materials Research Infrastructure (MARI) and Sustainable Fabrication (SusFab) at the University of Turku for infrastructure facilities. The authors acknowledge Azadeh Keshavarz for their assistance with dip coating experiments and Akseli Nykänen from the Department of Mechanical and Materials Engineering, University of Turku, for their assistance with the linear motor setup. Amit Barua is thankful to the Finnish Cultural Foundation and Turku University Foundation for providing financial support. During the preparation of this work, the authors used ChatGPT (OpenAI) to improve the readability and language of the manuscript and ChatGPT image generation (OpenAI) to assist in creating the conceptual illustration of the leaf skeleton in Figure 1a,b. The illustration is schematic only and does not represent experimental data. Following the use of these tools, the authors carefully reviewed and edited all content, verified the scientific accuracy of the figure and manuscript, and take full responsibility for the content of this publication.

Open access publishing facilitated by Turun yliopisto, as part of the Wiley - FinELib agreement.

Conflicts of Interest

The authors declare no conflicts of interest.

Data Availability Statement

The data that support the findings of this study are openly available in Zenodo at https://doi.org/10.5281/zenodo.18629701.

References

1. K. Li, Q. He, J. Wang, Z. Zhou, and X. Li, "Wearable Energy Harvesters Generating Electricity from Low-frequency human Limb Movement," *Microsystems & Nanoengineering* 4 (2018): 24, https://doi.org/10.1038/s41378-018-0024-3.

2. M. Jahandar, S. Kim, and D. C. Lim, "Transforming Wearable Technology with Advanced Ultra-Flexible Energy Harvesting and Storage Solutions," *Nature Communications* 15 (2024): 8149, https://doi.org/10.1038/s41467-024-52534-9.

3. L. Xiao, B. Yin, Z. Geng, J. Li, R. Jia, and K. Zhang, "Flexible Wearable Devices Based on Self-Powered Energy Supply," *Nano Energy* 142 (2025): 111157, https://doi.org/10.1016/j.nanoen.2025.111157.

4. H. Wu, Y. A. Huang, F. Xu, Y. Duan, and Z. Yin, "Energy Harvesters for Wearable and Stretchable Electronics: from Flexibility to Stretchability," *Advanced Materials* 28 (2016): 9881–9919, https://doi.org/10.1002/adma.201602251.

5. S. Saifi, X. Xiao, S. Cheng, et al., "An Ultraflexible Energy Harvesting-Storage System for Wearable Applications," *Nature Communications* 15 (2024): 6546, https://doi.org/10.1038/s41467-024-50894-w.

6. L. Dong, G. Hu, Q. Tang, C. Zhao, F. Yang, and Y. Yang, "Advanced Aerodynamics-Driven Energy Harvesting Leveraging Galloping-Flutter Synergy," *Advanced Functional Materials* 35 (2025): 2414324, https://doi.org/10.1002/adfm.202414324.

7. L. Dong, C. Zhao, S. Qu, et al., "Multi-Domain Energy Harvesting with Mode-Dependent Magneto-Mechano-Electric Coupling," *Advanced Energy Materials* 16 (2026): 06114, https://doi.org/10.1002/aenm.202506114.

8. X. Pu, M. Liu, X. Chen, et al., "Ultrastretchable, Transparent Triboelectric Nanogenerator as Electronic Skin for Biomechanical Energy Harvesting and Tactile Sensing," *Science Advances* 3, no. 5 (2017): 1700015.

9. D. Choi, Y. Lee, Z.-H. Lin, et al., "Recent Advances in Triboelectric Nanogenerators: from Technological Progress to Commercial Applications," *ACS Nano* 17 (2023): 11087–11219, https://doi.org/10.1021/acsnano.2c12458.

10. Z. Zhao, Y. Dai, D. Liu, et al., "Rationally Patterned Electrode of Direct-current Triboelectric Nanogenerators for Ultrahigh Effective Surface Charge Density," *Nature Communications* 11 (2020): 6186, https://doi.org/10.1038/s41467-020-20045-y.

11. V. T. Bui, T. H. Le, H. M. Jeong, et al., "Antagonistic-structured Breathable Triboelectric Nanogenerator Based on Sponge PMMA-GO/Electrode Mesh Hybrid for Wearable Healthcare Applications," *Nano Energy* 142 (2025): 111242, https://doi.org/10.1016/j.nanoen.2025.111242.

12. Y. Zi, J. Wang, S. Wang, et al., "Effective Energy Storage from a Triboelectric Nanogenerator," *Nature Communications* 7 (2016): 10987, https://doi.org/10.1038/ncomms10987.

13. K. Parida, G. Thangavel, G. Cai, et al., "Extremely Stretchable and Self-healing Conductor Based on Thermoplastic Elastomer for All-three-dimensional Printed Triboelectric Nanogenerator," *Nature Communications* 10 (2019): 2158.

14. K. R. S. Gunawardhana, N. D. Wanasekara, K. G. Wijayantha, and R. D. I. Dharmasena, "Scalable Textile Manufacturing Methods for Fabricating Triboelectric Nanogenerators with Balanced Electrical and Wearable Properties," *ACS Applied Electronic Materials* 4 (2022): 678–688, https://doi.org/10.1021/acsaelm.1c01095.

15. N. Wang, W. Zhang, Z. Li, et al., "Dual-electric-polarity Augmented Cyanoethyl Cellulose-based Triboelectric Nanogenerator with Ultra-high Triboelectric Charge Density and Enhanced Electrical Output Property at High Humidity," *Nano Energy* 103 (2022): 107748, https://doi.org/10.1016/j.nanoen.2022.107748.

16. G. S. dos Reis, H. P. de Oliveira, I. C. M. Candido, et al., "Supercapacitors and Triboelectric Nanogenerators Based on Electrodes of Greener Iron Nanoparticles/Carbon Nanotubes Composites," *Scientific Reports* 14 (2024): 11555.

17. J. Wang, Z. Zhang, S. Wang, et al., "Superstable Copper Nanowire Network Electrodes by Single-crystal Graphene Covering and Their Applications in Flexible Nanogenerator and Light-emitting Diode," *Nano Energy* 71 (2020): 104638, https://doi.org/10.1016/j.nanoen.2020.104638.

18. J. Zhao, Y. Wang, B. Wang, et al., "A Flexible and Stretchable Triboelectric Nanogenerator Based on a Medical Conductive Hydrogel for Biomechanical Energy Harvesting and Electronic Switches," *Nanoscale* 15 (2023): 6812–6821, https://doi.org/10.1039/D2NR05706A.

19. F. Invernizzi, S. Dulio, M. Patrini, G. Guizzetti, and P. Mustarelli, "Energy Harvesting from human Motion: Materials and Techniques," *Chemical Society Reviews* 45 (2016): 5455–5473, https://doi.org/10.1039/C5CS00812C.

20. L. Dong, Y. Ke, Y. Liao, et al., "Rational Modeling and Design of Piezoelectric Biomolecular Thin Films toward Enhanced Energy Harvesting and Sensing," *Advanced Functional Materials* 34 (2024): 2410566, https://doi.org/10.1002/adfm.202410566.

21. K. B. Anusha, D. K. Rane, S. S. D, N. K, V. D. Irudayaraj, and A. S. A. L. G. G. Gupta, "Energy Harvesting from Ambient Vibrations Using Piezoelectric Materials: a Sustainable Approach to Powering Iot Devices," *International Journal of Environmental Sciences* 11 (2025): 10–18, https://doi.org/10.64252/j5evd585.

22. N. Sun, X. N. Zhang, J. Z. Li, et al., "Waterproof, Breathable, and UV-Protective Nanofiber-Based Triboelectric Nanogenerator for Self-Powered Sensors," *ACS Sustainable Chemistry & Engineering* 11 (2023): 5608–5616, https://doi.org/10.1021/acssuschemeng.2c07643.

23. X. Zhang, X. Du, Y. Yin, et al., "Lithium-Ion Batteries: Charged by Triboelectric Nanogenerators with Pulsed Output Based on the Enhanced Cycling Stability," *ACS Applied Materials & Interfaces* 10 (2018): 8676–8684, https://doi.org/10.1021/acsami.7b18736.

24. G. Jian, S. Zhu, X. Yuan, et al., "Biodegradable Triboelectric Nanogenerator as a Implantable Power Source for Embedded Medicine Devices," *NPG Asia Materials* 16 (2024): 12, https://doi.org/10.1038/s41427-023-00528-2.

25. Y. Abid, A. Shuja, and I. Murtaza, "Nanofiber-based Triboelectric Nanogenerator Integrated with Supercapacitor Using Power Processing Circuit for Energy Harvesting Applications," *Journal of Materials Science: Materials in Electronics* 36 (2025): 1363.

26. H. Wu, C. Shan, S. Fu, et al., "Efficient Energy Conversion Mechanism and Energy Storage Strategy for Triboelectric Nanogenerators," *Nature Communications* 15 (2024): 6558, https://doi.org/10.1038/s41467-024-50978-7.

27. X. Peng, K. Dong, C. Ye, et al., "A Breathable, Biodegradable, Antibacterial, and Selfpowered Electronic Skin Based on all-nanofiber Triboelectric Nanogenerators," *Science Advances* 6 (2020): aba9624.

28. Z. Sun, F. Qin, Q. Sun, H. Zhu, and H. Wu, "Nature Inspired Structural Design for Local Optimization Management of Triboelectric Nanogenerators," *Advanced Functional Materials* 36 (2026): 19118, https://doi.org/10.1002/adfm.202519118.

29. M. Mayer, X. Xiao, J. Yin, G. Chen, J. Xu, and J. Chen, "Advances in Bioinspired Triboelectric Nanogenerators," *Advanced Electronic Materials* 8 (2022): 2200782, https://doi.org/10.1002/aelm.202200782.

30. M. A. A. Abdelkareem, X. Jing, M. Kamal Ahmed Ali, et al., "Recent Advances in Nature Inspired Triboelectric Nanogenerators for Self-powered Systems," *International Journal of Extreme Manufacturing* 6 (2024): 062003.

31. W. Li, Y. Pei, C. Zhang, and A. G. P. Kottapalli, "Bioinspired Designs and Biomimetic Applications of Triboelectric Nanogenerators," *Nano Energy* 84 (2021): 105865, https://doi.org/10.1016/j.nanoen.2021.105865.

32. B. Zhang, Y. Jiang, B. Chen, H. Li, and Y. Mao, "Recent Progress of Bioinspired Triboelectric Nanogenerators for Electronic Skins and Human–Machine Interaction," *Nanoenergy Advances* 4 (2024): 45–69, https://doi.org/10.3390/nanoenergyadv4010003.

33. V. Sharma, A. Koivikko, K. Yiannacou, K. Lahtonen, and V. Sariola, "Flexible Biodegradable Transparent Heaters Based on Fractal-Like Leaf Skeletons," *npj Flexible Electronics* 4 (2020): 27, https://doi.org/10.1038/s41528-020-00091-8.

34. V. Sharma, K. Jääskö, K. Yiannacou, A. Koivikko, V. Lampinen, and V. Sariola, "Performance Comparison of Fast, Transparent, and Biotic Heaters Based on Leaf Skeletons," *Advanced Engineering Materials* 24 (2022): 2101625, https://doi.org/10.1002/adem.202101625.

35. A. Barua, R. Gogoi, P. G. Reddy, et al., "Biomimetic Freestanding Microfractals for Flexible Electronics," *npj Flexible Electronics* 9 (2025): 10, https://doi.org/10.1038/s41528-025-00381-z.

36. A. Koivikko, V. Lampinen, K. Yiannacou, V. Sharma, and V. Sariola, "Biodegradable, Flexible and Transparent Tactile Pressure Sensor Based on Rubber Leaf Skeletons," *IEEE Sensors Journal* 22 (2022): 11241–11247, https://doi.org/10.1109/JSEN.2021.3078807.

37. A. Elsayes, V. Sharma, K. Yiannacou, A. Koivikko, A. Rasheed, and V. Sariola, "Plant-Based Biodegradable Capacitive Tactile Pressure Sensor Using Flexible and Transparent Leaf Skeletons as Electrodes and Flower Petal as Dielectric Layer," *Advanced Sustainable Systems* 4 (2020): 2000056, https://doi.org/10.1002/adsu.202000056.

38. X. Song, Y. Gu, S. Wang, J. Wang, and L. Yu, "Nanowire-Based Flexible Sensors for Wearable Electronics, Brain–Computer Interfaces, and Artificial Skins," *Electron* 3 (2025): 77, https://doi.org/10.1002/elt2.77.

39. J. Kwon, Y. D. Suh, J. Lee, et al., "Recent Progress in Silver Nanowire Based Flexible/Wearable Optoelectronics," *Journal of Materials Chemistry C* 6 (2018): 7445–7461, https://doi.org/10.1039/C8TC01024B.

40. X. Li, Y. Wang, C. Yin, and Z. Yin, "Copper Nanowires in Recent Electronic Applications: Progress and Perspectives," *Journal of Materials Chemistry C* 8 (2020): 849–872, https://doi.org/10.1039/C9TC04744A.

41. A. V. Nikolaeva, V. M. Kondratev, S. A. Kadinskaya, et al., "ZnO Nanowire-based Flexible Sensors for Pressure and Temperature Monitoring," *Materials Science in Semiconductor Processing* 189 (2025): 109253, https://doi.org/10.1016/j.mssp.2024.109253.

42. K. Keum, S. K. Park, and Y.-H. Kim, "Predictive Modeling of Optical and Electrical Coupling in Silver Nanowire Networks for Stretchable Transparent Electrodes," *Nanoscale* 18 (2026): 4199–4206.

43. J. Gu, Y. Shen, S. Tian, Z. Xue, and X. Meng, "Recent Advances in Nanowire-based Wearable Physical Sensors," *Biosensors* 13 (2023): 1025.

44. W. Zhang, H. Zhang, G. Chen, B. Ma, Y. Xia, and Y. Chen, "Bioinspired Leaf Vein-architected Gold Nanowire Ecoflexible Biosensors for Ultrasensitive Occlusal Force Monitoring," *Materials Horizons* 12 (2025): 6229–6240, https://doi.org/10.1039/D5MH00460H.

45. A. Barua and V. Sharma, "Biomimetic Breathable Surfaces for Triboelectric Nanogenerator for Energy Harvesting," in 2025 MIPRO 48th ICT and Electronics Convention (IEEE, 2025), 1739, https://doi.org/10.1109/MIPRO65660.2025.11131975.

46. B. Bagchi, P. Datta, C. S. Fernandez, et al., "Flexible Triboelectric Nanogenerators Using Transparent Copper Nanowire Electrodes: Energy Harvesting, Sensing human Activities and Material Recognition," *Materials Horizons* 10 (2023): 3124–3134, https://doi.org/10.1039/D3MH00404J.

47. X. Zha, D. Gong, W. Chen, L. Wu, and C. Zhang, "Synthesis of Copper Nanowires Using Monoethanolamine and the Application in Transparent Conductive Films," *Nanomaterials* 15 (2025): 638, https://doi.org/10.3390/nano15090638.

48. M. Nydegger, R. Deshmukh, E. Tervoort, M. Niederberger, and W. Caseri, "Composites of Copper Nanowires in Polyethylene: Preparation and Processing to Materials with NIR Dichroism," *ACS Omega* 4 (2019): 11223–11228, https://doi.org/10.1021/acsomega.9b01077.

49. H. Guo, H. Huang, S. Shi, et al., "Fabrication of Copper Nanowires Highly Conductive and Flexible Circuits by Direct Ink Writing," *Materials* 19 (2026): 618, https://doi.org/10.3390/ma19030618.

50. F. Jiang, S. Zheng, B. Hou, et al., "Printed Triboelectric Nanogenerator for Self-powered Devices: Ink Formulation of Printed Materials and Smart Integrated Devices," *Nano Energy* 121 (2024): 109224, https://doi.org/10.1016/j.nanoen.2023.109224.

51. D. H. Kim, J. H. Yu, C. Lee, et al., "Reconfiguring Hierarchical Porous Architecture of 2D Metal Nanosheets for Multifunctional Triboelectric Nanogenerators," *Advanced Materials* 38 (2025): 15466, https://doi.org/10.1002/adma.202515466.

52. J. H. Han and H. C. Moon, "Monolithically Integrated Ionic Triboelectric Nanogenerators for Deformable Energy Harvesting and Self Powered Sensing," *npj Flexible Electronics* 9 (2025): 114, https://doi.org/10.1038/s41528-025-00491-8.

53. Y. D. Suh, S. Hong, J. Lee, et al., "Random Nanocrack, Assisted Metal Nanowire-bundled Network Fabrication for a Highly Flexible and Transparent Conductor," *RSC Advances* 6 (2016): 57434.

54. B. Sun, R. Xu, X. Han, et al., "Ultra-high Temperature Tolerant Flexible Transparent Electrode with Embedded Silver Nanowires Bundle Micromesh for Electrical Heater," *npj Flexible Electronics* 6 (2022): 48, https://doi.org/10.1038/s41528-022-00182-8.

55. D. S. Hecht, L. Hu, and G. Irvin, "Emerging Transparent Electrodes Based on Thin Films of Carbon Nanotubes, Graphene, and Metallic Nanostructures," *Advanced Materials* 23 (2011): 1482–1513, https://doi.org/10.1002/adma.201003188.

56. W. Y. Chung, Y. C. Lai, T. Yonezawa, and Y. C. Liao, "Sintering Copper Nanoparticles with Photonic Additive for Printed Conductive Patterns by Intense Pulsed Light," *Nanomaterials* 9 (2019): 1071.

57. A. T. Bellew, H. G. Manning, C. Gomes da Rocha, M. S. Ferreira, and J. J. Boland, "Resistance of Single Ag Nanowire Junctions and Their Role in the Conductivity of Nanowire Networks," *ACS Nano* 9 (2015): 11422–11429, https://doi.org/10.1021/acsnano.5b05469.

58. M. Kanzaki, Y. Kawaguchi, and H. Kawasaki, "Fabrication of Conductive Copper Films on Flexible Polymer Substrates by Low-Temperature Sintering of Composite Cu Ink in Air," *ACS Applied Materials & Interfaces* 9 (2017): 20852–20858, https://doi.org/10.1021/acsami.7b04641.

59. R. Pan, W. Xuan, J. Chen, et al., "Fully Biodegradable Triboelectric Nanogenerators Based on Electrospun Polylactic Acid and Nanostructured Gelatin Films," *Nano Energy* 45 (2018): 193–202, https://doi.org/10.1016/j.nanoen.2017.12.048.

60. G. Khandelwal, G. Min, X. Karagiorgis, and R. Dahiya, "Aligned PLLA Electrospun Fibres Based Biodegradable Triboelectric Nanogenerator," *Nano Energy* 110 (2023): 108325, https://doi.org/10.1016/j.nanoen.2023.108325.

61. V. Sabzevari, M. Mahdi Abolhasani, and S. Azimi ab, "A Fully Biocompatible and Biodegradable Triboelectric Nanogenerator Based on PVA/Chitosan Fibers and PLA Fibers with Enhanced Output Performance," *Journal of Materials Chemistry C* 14 (2026): 5034–5044, https://doi.org/10.1039/D5TC03882K.

62. Q. Xie, Z. Yan, S. Wang, et al., "Transparent, Flexible, and Stable Polyethersulfone/Copper-Nanowires/Polyethylene Terephthalate Sandwich-Structured Films for High-Performance Electromagnetic Interference Shielding," *Advanced Engineering Materials* 23 (2021): 2100283, https://doi.org/10.1002/adem.202100283.

63. A. Barua, R. Gogoi, P. G. Reddy, et al., "Biomimetic Freestanding Microfractals for Flexible Electronics," *npj Flexible Electronics* 9 (2025): 1, https://doi.org/10.1038/s41528-025-00381-z.

64. M. Matic, A. Miljavac, V. Sharma, and M. Poljak, "Resistivity Modeling of Copper Nanowires with Sub-100 Nm Diameter," (2025): 1714, https://doi.org/10.1109/MIPRO65660.2025.11131863.

65. E. H. Sondheimer, "The Mean Free Path of Electrons in Metals," *Advances in Physics* 1 (1952): 1–42, https://doi.org/10.1080/00018735200101151.

66. A. F. Mayadas and M. Shatzkes, "Electrical-Resistivity Model for Polycrystalline Films: the Case of Arbitrary Reflection at External Surfaces," *Physical Review B* 1 (1970): 1382–1389, https://doi.org/10.1103/PhysRevB.1.1382.

Supporting Information

Additional supporting information can be found online in the Supporting Information section.

Supporting File 1: adfm77314-sup-0001-SuppMat.docx.

Supporting File 2: adfm77314-sup-0002-VideoS1.mp4.

Supporting File 3: adfm77314-sup-0003-VideoS2.mp4.

Supporting File 4: adfm77314-sup-0004-VideoS3.mp4.

Supporting File 5: adfm77314-sup-0001-VideoS4.mp4.

Supporting File 6: adfm77314-sup-0006-VideoS5.mp4.

Supporting File 7: adfm77314-sup-0007-VideoS6.mp4.